MOEM

Modern Electronic Materials 4(3): 87–95
DOI 10.3897/j.moem.4.3.39540

Review Article

Structure and electrical properties of zinc oxide base iron doped ceramics

Alexey V. Pashkevich[1,3], Aleksandr K. Fedotov[1,3], Yuliya V. Kasyuk[1], Liudmila A. Bliznyuk[2], Julia A. Fedotova[1], Nikita A. Basov[2], Alexander S. Fedotov[3], Ivan A. Svito[3], Evgheni N. Poddenezhny[4]

1 Research Scientific Institute for Nuclear Problems of Belarusian State University, 11 Bobruiskaya Str., Minsk 220030, Belarus

2 National Practical Center of National Academy of Science of for Material Science, 19 P. Brovka Str., Minsk 220072, Belarus

3 Belarusian State University, 4 Nezavisimosti Ave, 220030 Minsk, Belarus

4 P.O. Sukhoi Gomel State Technical University, 48 Oktyabrya Ave, Gomel 246746, Belarus

Corresponding author: *Alexander S. Fedotov* (fedotov@bsu.by)

Received 16 May 2018 ♦ **Accepted** 3 August 2018 ♦ **Published** 1 September 2018

Citation: Pashkevich AV, Fedotov AK, Kasyuk YV, Bliznyuk LA, Fedotova JA, Basov NA, Fedotov AS, Svito IA, Poddenezhny EN (2018) Structure and electrical properties of zinc oxide base iron doped ceramics. Modern Electronic Materials 4(3): 87–95. 10.3897/j.moem.4.3.39540

Abstract

The search for new economically advantageous technologies of new zinc oxide based composite ceramic materials and the study of their structure and properties attract special attention today. These ceramics have a number of advantages as compared with materials prepared by more expensive technologies, due to the possibility to fabricate items having different shapes and sizes and particularly to vary their morphology, structure and phase composition. This allows controlling their functional properties by varying the powder particle size in charge, the temperatures, durations and atmospheres of synthesis and heat treatment, and the types of doping impurities in the ceramics. The structure and electrical properties of $(Fe_xO_y)_{10}(ZnO)_{90}$ ceramics ($0 \le x \le 3$; $1 \le y \le 4$) synthesized in air using single- and two-stage synthesis methods have been studied. FeO, α-Fe_2O_3 and Fe_3O_4 powders or (α-Fe_2O_3 + FeO) mixture have been used for ZnO doping. X-ray diffraction, gamma-ray resonance spectroscopy and Raman spectroscopy data suggest that at average iron concentrations of 1–3 at.% the ceramic specimens contain at least three phases: the $Zn_{1-\delta}Fe_\delta O$ solid solution with a wurtzite structure, the $ZnFe_2O_4$ ferrite phase with a spinel structure and Fe_xO_y residual iron oxides which were used as doping impurities. Scanning electron microscopy and energy dispersion X-ray analysis have shown that the wurtzite phase grain size in the ceramic specimens decreases from several decades of microns for single-stage synthesis to submicron sizes for two- stage synthesis. We show that iron addition to ZnO induces a compression of the wurtzite phase crystal lattice, the compression of lattice magnitude being proportional to the oxygen content in the Fe_xO_y iron oxide doping agent. The temperature dependences of the electrical resistivity suggest that deep donor centers with an activation energy of about 0.37 eV are formed in the $Zn_{1-\delta}Fe_\delta O$ wurtzite phase. The temperature dependences of the electrical resistivity of electrons for undoped ZnO in the 6–300 K range and for doped $(FeO)_{10}(ZnO)_{90}$ ceramic synthesized in one stage exhibit a variable activation energy below 50 K which indicates a heavily disordered structure.

Keywords

zinc oxide, ceramics, iron doping, phase structure, electrical properties

1. Introduction

The search for new economically advantageous technologies and the study of the structure and properties of new zinc oxide base composite ceramic materials currently draw special attention [1]. These ceramics have a number of advantages over materials the technologies of which are more expensive, due to the possibility to fabricate items having different shapes and sizes and particularly to vary their morphology, structure and phase composition. This allows controlling their functional properties by varying the powder particle size of the charge, the temperatures, durations and atmospheres of synthesis as well as following heat treatment and the types of doping impurities in the ceramics [2–4].

Zinc oxide can be used as the base material for the fabrication of conventional devices (e.g. variable resistors [2]) or fundamentally new device types. For example, ZnO doping with magnetic impurities allows producing promising materials having novel electronic, optical and magnetic properties [5–12] including magnetic field controlled ones [13, 14].

Zinc oxide base composite ceramics can be used for the fabrication of thermoelectric transducers [15], yet this will require increasing their electrical conductivity and reducing their heat conductivity which can be achieved e.g. by doping.

Doping of ZnO base composite ceramic materials with transition elements is of special research interest [5–12]. The properties of these materials depend not only on the concentration of incorporated impurities but also on whether they are distributed in the matrix lattice (wurtzite) homogeneously or form submicron size magnetic clusters with a specific phase and magnetic structure. Hybrid nanocomposite structures of this type can be used for the fabrication of various devices e.g. adsorption gas sensors [16–20].

There are numerous literary experimental data on the effect of doping with transition or other elements on the structure and properties of single crystals, polycrystalline films, nanostructured powders, nanowires or tetrapods [5–12, 21–23]. However, ZnO base compositions synthesized using ceramic technologies have not yet been studied completely (except ceramics for variable resistors and optical applications [2, 7]). The effect of magnetic impurities (including iron) in ZnO base ceramic compositions and variation of synthesis conditions on the chemical composition, structure and magnetic properties of the forming phases has not yet been studied in the required detail. Furthermore there is insufficient information on the effect of the type of the forming intrinsic defects and defect complexes on the electron transport and other properties of the ceramics. Iron often incorporates in zinc oxide during the growth and is one of the most abundant d-group transition metal impurities in this material [21, 24–26]. Calculations [27] showed that in the perfect ZnO the iron ions having the Fe^{2+} charge state should give relatively shallow donors. However the presence of random acceptors in real specimens (e.g. nitrogen for ZnO synthesized in air) transforms Fe^{2+} to Fe^{3+} leading to the formation of deep donor levels [27].

The aim of this work is to study the effect of synthesis method and type of doping agents (Fe_xO_y iron oxides) on the phase composition and electrical properties of ZnO base ceramics.

2. Materials and experimental

The ZnO base specimens were synthesized using the conventional open air powder sintering technique for ceramics [2, 7]. The source components for charge preparation were ultrahigh-purity ZnO, FeO, α-Fe_2O_3 and Fe_3O_4 powders and (α-Fe_2O_3 + FeO) mixtures (Table 1). The weights of the charge components in the studied specimens were calculated using the $(Fe_xO_y)_{10}(ZnO)_{90}$ compound formula in which the weight fraction of the iron oxide powders was 10 wt.%.

Table 1. Specimen synthesis methods.

Spec. No.	Specimen*	Synthesis method	Preliminary/Final Sintering	
			Temperature, °C	Time, h
1	ZnO	Sintering	1100	2
2	$(ZnO)_{90}(FeO)_{10}$-1	Single-Stage Synthesis	1200	2
3	$(ZnO)_{90}(Fe_2O_3)_{10}$-1			
4	$(ZnO)_{90}(Fe_3O_4)_{10}$-1			
5	$(ZnO)_{90}(FeO)_{10}$-2	Two-Stage Synthesis	900/1200	2/2
6	$(ZnO)_{90}(Fe_2O_3)_{10}$-2			
7	$(ZnO)_{90}(Fe_3O_4)_{10}$-2			
8	$(ZnO)_{90}(Fe_2O_3 + FeO)_{10}$-2	Two-Stage Synthesis		4/48

*"1" and "2" in the specimen notations refer to single- and two-stage synthesis, respectively.

The powders were mixed in a stainless steel attritor with hard-alloy balls in the presence of a humidifier (alcohol). The initial oxide particle sizes (as-grinded for 12 h) were 10–50 μm. For charge preparation the source oxides were dried at 500–900 °C approaching constant weight, following which 3 wt.% PVA glue binder was added to the charge. Then the mixture was uniaxially compacted at 200 MPa to 10–18 mm diam. 2–5 mm thickness tablets. For single-stage synthesis the as-compacted tablets were sintered in air at 1200 °C for 2 h. For two-stage synthesis the tablets were preliminarily sintered at 900 °C for 2 h, then ground again to powder, mixed with the binder, compacted and annealed in open air at 1200 °C for 2 h. As can be seen from Table 1 the synthesis method for Ceramic No. 8 differed from the others. After synthesis or annealing the specimens were cooled in the furnace at a 200–300 K/h rate.

The structure and phase composition of the ceramics were studied at room temperature using X-ray diffraction (XRD) on a DRON-3 M automated instrument in CuK_α radiation and using scanning electron microscopy (SEM) in secondary electron mode on Oxford Instruments LEO

1455VP and Tescan Vega 3LMU instruments. The 20 scanning step for XRD was max. 0.03, the exposure time being min. 5 sec. The X-ray diffraction patterns were processed using the FullProf software based on the Ritweld profile analysis method [28].

The element concentrations in the composites were measured using selected area electron probe X-ray analyzers for energy dispersive X-ray analysis (EDXA) installed on the scanning electron microscope.

The porosity of the specimens was studied under an Olimpus GX41 microscope (Japan) with the AutoScan 005 software.

Mössbauer spectra were taken in the 20–300 K range on an MS4 Mössbauer spectrometer (SEE Co., USA) for powdered specimens (^{57}Fe isotope, transmission mode, ^{57}Co/Rh source (20 mCi)). The spectra were approximated using the Rancourt method based MOSMOD software [29].

Raman spectra were taken on a Nanofinder High-End LOTIS TII confocal spectrometer (Belarus, Japan). The signal was excited with a solid state laser (532 nm, 20 mW). The laser radiation was focused on the specimen surface with a 50$^{\times}$ objective (digital aperture 0.8+). The incident laser radiation power was reduced to 2 mW for the avoidance of heat damage. The backscattered light was dispersed by a 600 mm^{-1} diffraction grating for achieving a spectral resolution of not worse than 3 cm^{-1}. Spectral calibration was based on gas discharge lamp lines for achieving an accuracy of not worse than 3 cm^{-1}. The signal acquisition time was 30 s. The photodetector was a cooled silicon CCD matrix.

The temperature dependences of the electrical resistivity $\rho(T)$ of the ceramics were measured for rectangular specimens (2–3 mm in width and thickness and 7–10 mm in length) cut out from the synthesized ceramic tablets, with silver current and potential contacts deposited on the specimen surfaces. The $\rho(T)$ curves were measured on a High Field Measurement System instrument (Cryogenic Ltd, London) in the 6–300 K range. The test specimens were mounted in a special probe with a system of thermometers and heaters. The probe with soldered-up specimens was placed in a close-cycle refrigerator cryostat with a superconducting solenoid and connected to the automatic measurement system.

The current passing through the specimen was controlled with a Keithley 6430 Sub-Femtoamp Remote SourceMeter which provided for specimen electrical resistivity measurements in the 100 μOhm – 20 GOhm range with an accuracy of not worse than 0.1%. The specimen temperature was controlled with LakeShore thermal diodes calibrated accurate to a 0.0005 K and having a reproducibility of 0.001 K thus allowing temperature stabilization and measurement with an accuracy of not worse than 0.005 K using a LakeShore 331 measurement controller. The relative error of the electrical resistivity measurements was within 5%, being mainly determined by the specimen dimension measurement error and the sizes of the electric potential contacts.

3. Results and discussion

3.1. Structure and phase composition of composite ceramics

Table 2 shows types and weight fractions of doping oxides and main structural parameters of the test ceramics: porosity, EDXA-determined specimen-average iron concentration and average δ-iron concentration in the solid solution of the main (wurtzite) $Zn_{1-\delta}Fe_{\delta}O$ phase, average Fe concentration in sample and concentration (delta) in Wurtzite phase and lattice parameters of the ferrite phase and residual doping impurities forming during the synthesis.

Figure 1 shows typical examples of SEM cleavage surface images for single- and two-stage synthesized ceramic specimens. It can be seen from Fig. 1 that the grain size of the single-stage synthesized ceramics ranges from several to decades of microns (Fig. 1 *a*, *c*, *e*, *g*). After two-stage synthesis the predominant grain size decreased to the submicron range (Fig. 1*b*, *d*, *f*, *h*) although as can be seen from Fig. 1*b*, *d* some large grains persisted after the second synthesis stage. The

Table 2. Main structural parameters of the specimens.

No.	Specimen	Porosity	Average Fe concentration in ZnO, at.%	Fe(δ) concentration in $Zn_{1-\delta}Fe_{\delta}O$, at.%	Lattice parameters, nm	
					Wurtzite phase	Ferrite phase
1	ZnO	14.6	0	0	$a = 0.32498$	
					$c = 0.52020$	–
2	$(ZnO)_{90}(FeO)_{10}$-1	17.0	1.2	0.77	$a = 0.32595$	
					$c = 0.52073$	–
3	(ZnO)90(Fe2O3)10-1	15.5	2.3	0.82	$a = 0.32381$	
					$c = 0.51822$	–
4	(ZnO)90(Fe3O4)10-1	18.7	2.87	0.69	$a = 0.32372$	
					$c = 0.51805$	–
5	$(ZnO)_{90}(FeO)_{10}$-2	18.3	1.0	0.81	$a = 0.32418$	0.83892
					$c = 0.51900$	
6	$(ZnO)_{90}(Fe_2O_3)_{10}$-2	17.1	2.81	0.66	$a = 0.32367$	0.84074
					$c = 0.51809$	
7	(ZnO)90(Fe3O4)10-2	16.5	2.98	0.79	$a = 0.32377$	
					$c = 0.51835$	0.84322
8	(ZnO)90(Fe2O3 + FeO)10-2	17.0	5.04	0.87	$a = 0.32346$	
					$c = 0.51758$	0.84077

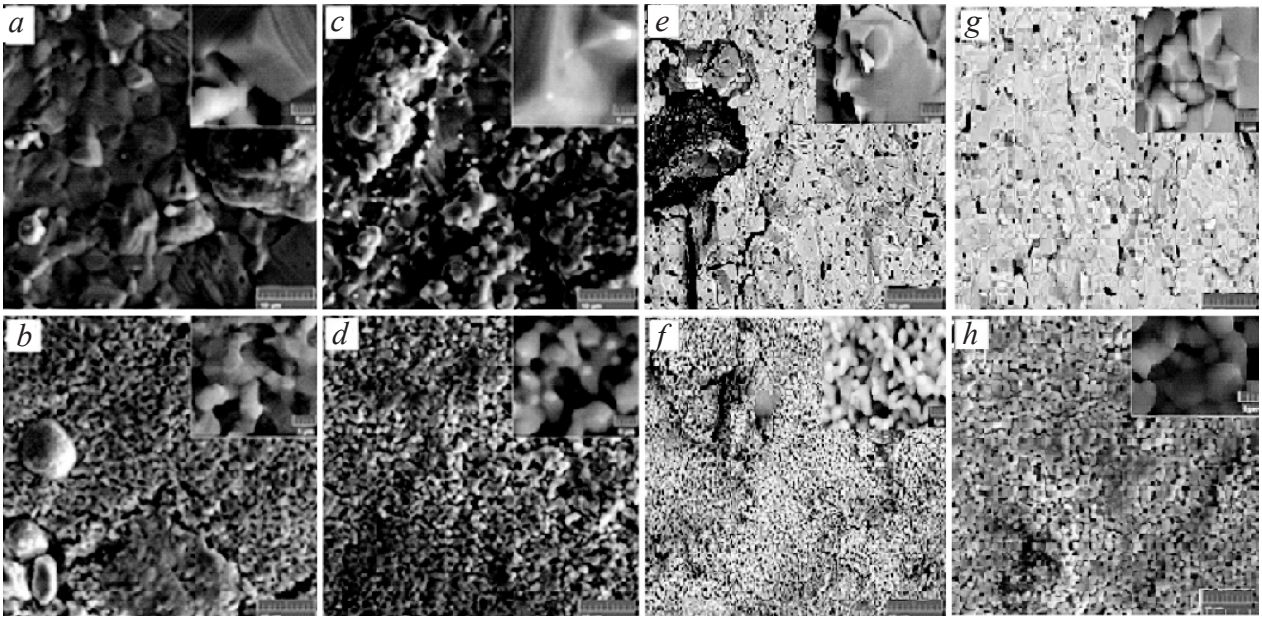

Figure 1. Typical SEM images of the grain structure at the cleavage surfaces of $(Fe_xO_y)_{10}(ZnO)_{90}$ ceramics synthesized using (*a*, *c*, *e*, *g*) single-stage synthesis method and (*b*, *d*, *f*, *h*) two-stage synthesis method with the doping impurities being (*a* and *b*) FeO, (*c* and *d*) α-Fe_2O_3, (*e* and *f*) Fe_3O_4 and (*g* and *h*) Fe_2O_3. Inset: Large magnification SEM images of separate specimen areas.

XRD study showed that the wurtzite structure remained in the $Zn_{1-\delta}Fe_\delta O$ solid solutions regardless of the Fe_xO_y doping impurity type. According to the EDXA data presented in Table 2 the iron content in the wurtzite phase solid solution of most ceramics studied was in the $0.66 < \delta < 0.81$ at.% range. The only exclusion was ceramic Specimen No. 8 synthesized at a higher temperature and during a longer time.

According to the XRD data the $(Fe_xO_y)_{10}(ZnO)_{90}$ doped ceramics contained, along with the $Zn_{1-\delta}Fe_\delta O$ wurtzite structure solid solution lines, several additional peaks marked with arrows in Fig. 2. The lattice parameters of the phases calculated by approximation from the XRD spectra are also shown in Table 2. The observed decrease in the *a* and *c* lattice parameters of the wurtzite phase after ZnO doping seems to be caused by partial substitution of Zn ions for iron ones in this phase. It should also be noted that the *a*/*c* lattice parameter ratio remains almost the same for all the doping impurities studied, i.e. the cell is not distorted.

Based on X-ray pattern fitting we can attribute the additional peaks (marked with arrows in Fig. 2) to the $ZnFe_2O_4$ ferrite phase and residual Fe_xO_y iron oxides.

The presence of additional phases in the $(Fe_xO_y)_{10}(ZnO)_{90}$ composite ceramic structure (along with $Zn_{1-\delta}Fe_\delta O$ solid solutions having a wurtzite structure) was also detected by EDXA, Mössbauer and Raman spectroscopies. EDXA showed that $Zn_{1-\delta}Fe_\delta O$ solid solution grains with $\delta < 1$ at.% (dark regions in Fig. 3) coexist with relatively large regions (5–30 μm or even larger) containing 2–3 wt.% iron (bright regions in Fig. 3). According to Table 1, the presence of these iron-rich regions with a $ZnFe_2O_4$ ferrite structure and/or Fe_xO_y residual oxides increases the average iron content in the $(Fe_xO_y)_{10}(ZnO)_{90}$ ceramic specimens to 1–3 at.%.

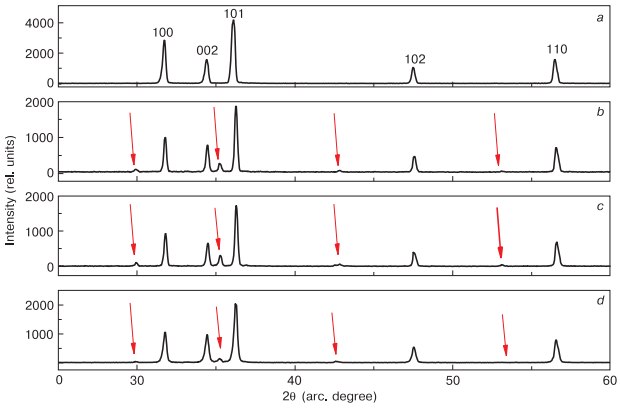

Figure 2. Typical XRD spectra for undoped ZnO and $(Fe_xO_y)_{10}(ZnO)_{90}$ composite ceramics synthesized in two stages using different Fe_xO_y doping impurities: (*a*) ZnO, (*b*) $(ZnO)_{90}(FeO)_{10}$-2, (*c*) $(ZnO)_{90}(Fe_2O_3)_{10}$-2 and (*d*) $(ZnO)_{90}(Fe_3O_4)_{10}$-2. Figure 2a shows Miller's indices for the zinc oxide wurtzite lattice. Arrows in Fig. 2b–d show the additional peaks observed in the spectra corresponding to the $ZnFe_2O_4$ ferrite phase or Fe_xO_y residual oxides.

The Raman spectra of the specimens also suggest the presence of not only the wurtzite phase (Fig. 4) but also additional iron containing phases (Fig. 5). Comparison of the Raman peak positions in Fig. 5 with literary data [23] suggests the presence of two cubic phases one of which is identified as $ZnFe_2O_4$ zinc ferrite and the others can be interpreted as residual source Fe_xO_y doping impurities.

The Mössbauer data confirm the XRD, EDXA and Raman data indicating the presence of additional phases with high iron content in the experimental ceramic specimens. To analyze the phase transformations occurring during the synthesis of the composite ceramics studied we measured the Mössbauer spectra both for the initial

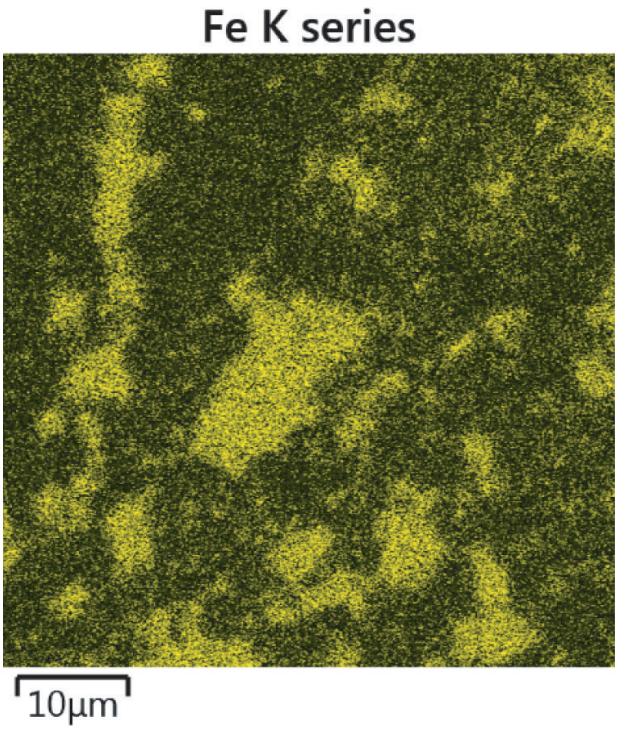

Figure 3. Example of EDXA iron distribution in $(ZnO)_{90}(FeO)_{10}$-2 composite ceramic (Table 1, Specimen 5).

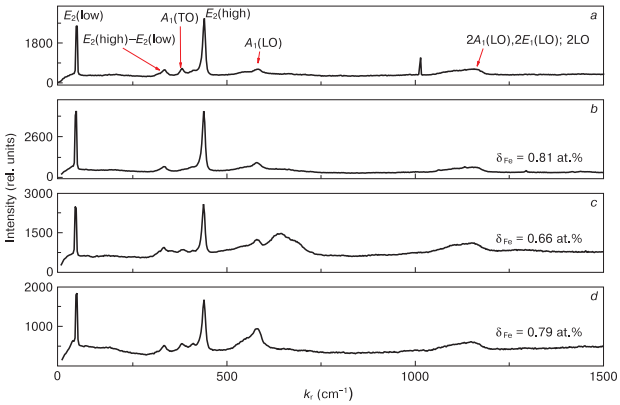

Figure 4. Examples of Raman spectra for the wurtzite phase in (*a*) indoped ZnO and (*b*) $(ZnO)_{90}(FeO)_{10}$-2, (*c*) $(ZnO)_{90}(Fe_2O_3)_{10}$-2 and (*d*) и $(ZnO)_{90}(Fe_3O_4)_{10}$-2 doped composite ceramics.

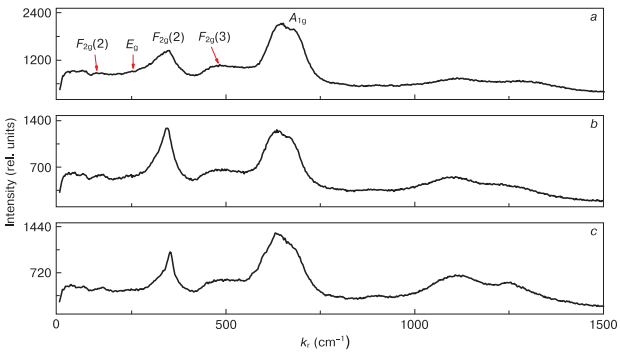

Figure 5. Examples of Raman spectra for phase inclusions in (*a*) $(ZnO)_{90}(FeO)_{10}$-2, (*b*) $(ZnO)_{90}(Fe_2O_3)_{10}$-2 and (*c*) $(ZnO)_{90}(Fe_3O_4)_{10}$-2 composite ceramics.

powder mixtures before compacting and for the as-synthesized ceramic specimens with different doping impurities for single- and two-stage synthesis methods (Fig. 6).

As can be seen from Fig. 6 *a* and *b* the Mössbauer spectra of the source powders mixtures ((*a*) $(ZnO)_{90}(\alpha\text{-}Fe_2O_3)_{10}$ and (*b*) $(ZnO)_{90}(Fe_3O_4)_{10}$) contain magnetically split sextets [31]. The $(ZnO)_{90}(FeO)_{10}$ powder mixture also proved to exhibit a magnetically split sextet. The Mössbauer spectra of all the as-synthesized ceramic specimens changed significantly and mainly contained a non-magnetic doublet (Fig. 6b, d) pertaining to $ZnFe_2O_4$ zinc ferrite [30] which was also detected in these ceramics by EDXA (Fig. 3).

3.2. Electrical properties of composite ceramics

Below we present the electrical properties of the $(Fe_xO_y)_{10}(ZnO)_{90}$ ceramics depending on the synthesis method (single- or two stage) and Fe_xO_y doping impurity type. The room temperature electrical resistivity ρ_{300} data for the specimens are summarized in Table 3. Figure 7 shows the temperature dependences of the electrical resistivity $\rho(T)$ for undoped (Curve *1*) and doped (Curves *2–8*) ceramic specimens.

As can be seen from Fig. 7, zinc oxide doping with iron leads to an increase in the electrical resistivity near room temperature ρ_{300} for most of the specimens. The only exclusion is the $(ZnO)_{90}(FeO)_{10}$-1 specimen synthesized in one stage whose electrical resistivity at $T > 200$ K proved to be lower than that of the undoped ZnO specimens which, as follows from Fig. 7, is most likely due to its heavily inhomogeneous structure.

By and large, as can be seen from Fig. 7 the $(Fe_xO_y)_{10}(ZnO)_{90}$ specimens can be divided in two groups by $\rho(T)$ dependence pattern.

One group (Curves *3–7*) have linear (Ln ρ) dependences on inverse temperature ($1/T$) in Arrhenius coordinates in the 150–300 K range. These specimens include all the two-stage synthesized ceramics and those of the single-stage synthesized ones which were doped with Fe_2O_3 or Fe_3O_4 oxides or ($FeO + Fe_2O_3$) mixture. The linear sections of the Lg ρ – ($1/T$) functions for the specimens have close conductivity activation energies $\Delta E_\sigma \approx 0.37$ eV as determined from the linear section slopes of the Ln $\rho(1/T)$ curves in Fig. 7.

The second group of curves in Fig. 7 (Specimens 1, 2 and 8) refer to undoped zinc oxide ceramics (Specimen 1) and $(FeO)_{10}(ZnO)_{90}$ specimens synthesized using the single-stage (Specimen 2) and two-stage (Specimen 8) methods which had lower resistivities at $T > 150$ K as noted above. As can be seen from Fig. 7, Specimens 1, 2 and 8 have cooling-reduced conductivity activation energy which is in the 0.005–0.05 eV range at 6–50 K.

We will now discuss the experimental data on the structure and electrical properties of the ceramics. Table 3 suggests that in the 150–300 K range the temperature dependences of the electrical resistivity of iron doped ceramics 3–8 obey the following law:

$$\rho(T) = \rho_{03} \exp\left(-\frac{\Delta E_\sigma}{kT}\right), \qquad (1)$$

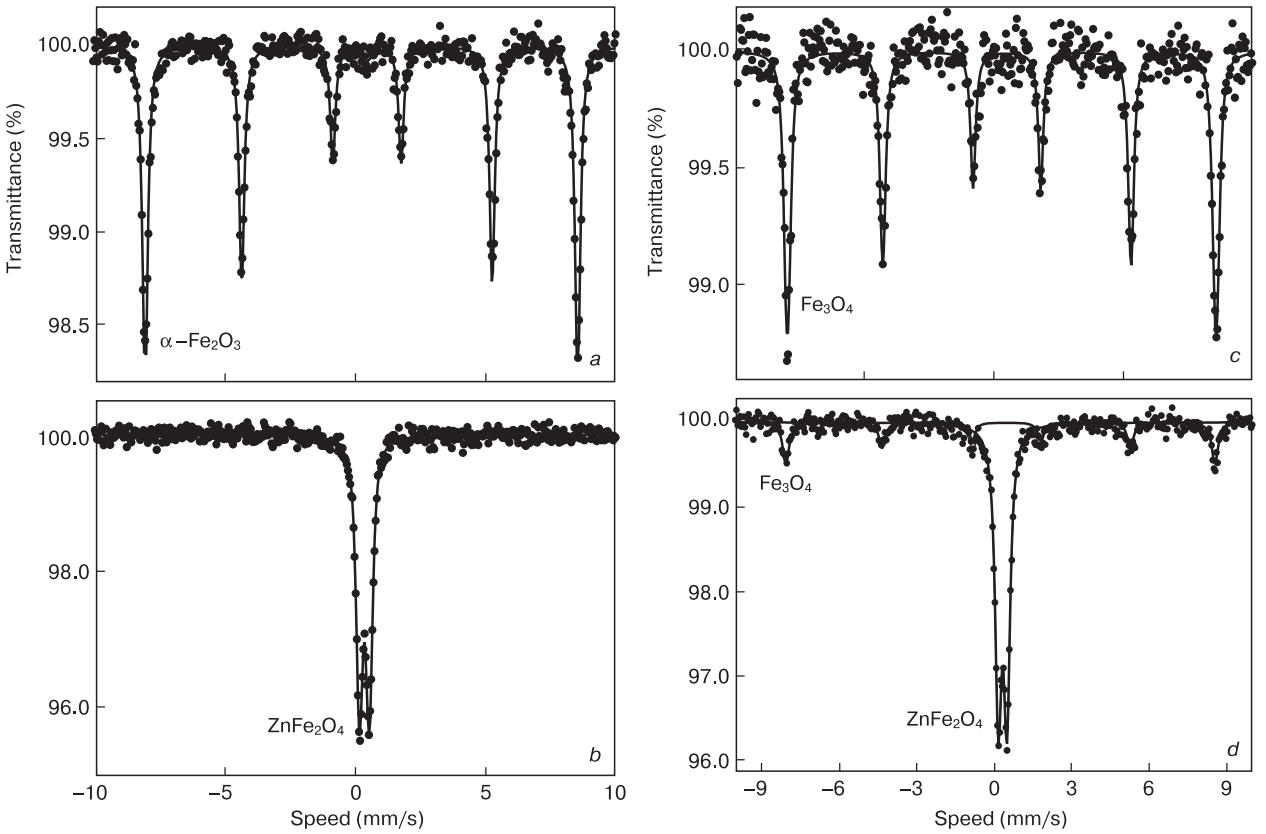

Figure 6. Mössbauer spectra of (*a*) $(ZnO)_{90}(\alpha\text{-}Fe_2O_3)_{10}$ and (*c*) $(ZnO)_{90}(Fe_3O_4)_{10}$ initial powders and (*b*) $(ZnO)_{90}(Fe_2O_3)_{10}$-2 and (*d*) $(ZnO)_{90}(Fe_3O_4)_{10}$-2 respective composite ceramics synthesized in two stages.

Table 3. Main electrical parameters of the specimens.

No.	Specimen	Average Fe concentration in $(Fe_xO_y)_{10}(ZnO)_{90}$, at.%	Fe(δ) concentration in $Zn_{1-\delta}Fe_\delta O$, at.%	ρ at 300 K, Ohm · m	ΔE_σ at 300 K, eV
1	ZnO	0	0	$3.67 \cdot 10^1$	0.05–0.07
2	$(ZnO)_{90}(FeO)_{10}$-1	1.2	0.77	$7.51 \cdot 10^0$	0.36
3	$(ZnO)_{90}(Fe_2O_3)_{10}$-1	2.3	0.82	$1.32 \cdot 10^0$	0.27
4	$(ZnO)_{90}(Fe_3O_4)_{10}$-1	2.87	0.69	$2.86 \cdot 10^5$	0.34
5	$(ZnO)_{90}(FeO)_{10}$-2	1.0	0.81	$7.89 \cdot 10^2$	0.36
6	$(ZnO)_{90}(Fe_2O_3)_{10}$-2	2.81	0.66	$3.18 \cdot 10^3$	0.37
7	$(ZnO)_{90}(Fe_3O_4)_{10}$-2	2.98	0.79	$6.12 \cdot 10^2$	0.37
8	$(ZnO)_{90}(FeO + Fe_2O_3)_{10}$-2	5.04	0.87	$4.37 \cdot 10^1$	0.24

with the conductivity activation energy ΔE_σ ~0.37 eV. This E_σ value is far greater than the literary data, i.e., 0.25 ± 0.02 for polycrystalline ZnO films with 0.2 wt.% iron content, which were attributed [26] to the Fe^{3+} ionization energy.

Note that multiple researchers reported ionization or conductivity activation energies of ~0.15–0.4 eV for undoped zinc oxide which were attributed to the presence of the impurity band and/or tails of localized states [32] and to intrinsic donor defects [33–35] (e.g. zinc vacancies forming during ceramic sintering in air). On the other hand the experimentally revealed deep level can be associated with the formation of the Fe–O complexes during ceramic synthesis and heat treatment. This should increase the concentration of oxygen vacancies which are formed due to leaving by oxygen of zinc oxide lattice sites towards iron ions. However, taking into account

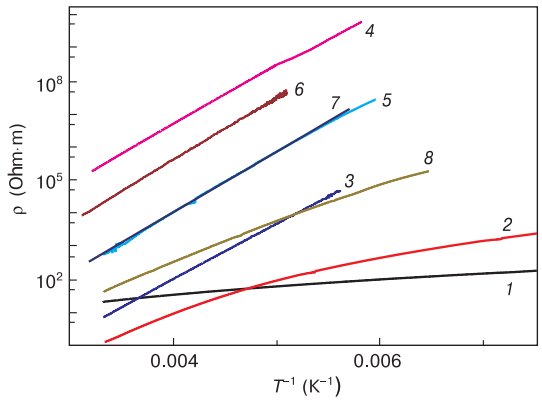

Figure 7. Temperature dependences of electrical resistivity for (*1*) undoped and (*2–8*) doped $(ZnO)_{90}(Fe_xO_y)_{10}$ ceramic specimens. Curve numbering corresponds to specimen numbering in Table 3.

the doping level of the experimental specimens (above 10^{20} m^{-3} for the wurtzite phase), the revealed deep donor centers could as well be attributed to the presence of some quantity of double-charged iron ions [36]. The deep donor was reported [36] to originate from the interaction of solute Fe^{2+} iron ions with the intrinsic defects (e.g. due to the incorporation of these ions into the zinc sublattice) in the wurtzite crystal lattice which however is in conflict with our Mössbauer data.

As noted above the $\rho(T)$ dependences in Arrhenius coordinates for the undoped specimens and a doped one (Fig. 7 Curves *1* and *2*) suggest that the activation energy decreases with decreasing temperature. This is commonly attributed either to electron hopping through localized states with variable hopping range (the so-called VHR mode) or to the presence of tails of localized states or large-scale potential relief caused by an inhomogeneous distribution of impurities and defects. The electron hopping conductivity is described by the well-known Mott relationship [32, 37].

$$\rho(T) = \rho_{01} \exp\left[-\left(\frac{T_0}{T}\right)^{\alpha}\right], \qquad (2)$$

where $\alpha = 0.25$ for Mott's mechanism in bulk semiconductors and $\alpha = 0.5$ for Shklovskii-Efros' hopping. The ρ_{01} and T_0 parameters in Eq. (2) are the characteristic parameters of the respective VHR hopping conductivity mode.

The relevance of the $\rho(T)$ curves to some variant of Eq. (2) usually becomes clear from their representation in the so-called Mott coordinates Ln $\rho - (1/T)^{\alpha}$. As can be seen from Fig. 8 *b* the Mott representation of the $\rho(T)$ curves for temperatures below 15 K causes linearization of the $\rho(T)$ curves over a wider range of low temperatures in accordance with the Shklovskii-Efros law [37]. This indicates possible formation of the Coulomb gap in the vicinity of the Fermi level for VHR conductivity through localized states. A similar behavior was observed for polycrystalline films [39]. It should be noted that the linearization of the $\rho(T)$ curves in Mott's coordinates was absent for doped Specimen No. 2.

As can be seen from Curve *1* in Fig. 8 *a* heating of the undoped ceramic specimen to 20 K < T < 40 K initiates a $\rho(T)$ curve transition from the Shklovskii-Efros law to the Mott law with $\alpha = 0.25$ in Eq. (2). Above 50 K, undoped ZnO and the heavily inhomogeneous doped single-stage synthesized specimens (Fig. 9 *a*, Curve *2*) exhibit a $\rho(T)$ curve transition to dependences of the following type

$$\rho(T) = \rho_{02} \exp\left(-\frac{\Delta E}{kT}\right), \qquad (3)$$

where the conductivity activation energy $\Delta E \approx (E_p - E_F)$ is not equal to the impurity ionization energy and is temperature dependent. Here E_F is the Fermi level and E_p is the percolation level. These dependences are typically attributed to specimen inhomogeneity [39, 40] and often observed in polycrystalline undoped zinc oxide films [34, 35].

As noted above the $\rho(T)$ curve pattern described by Eq. (3) is often associated with the formation of tails of localized states near the conduction band bottom and the

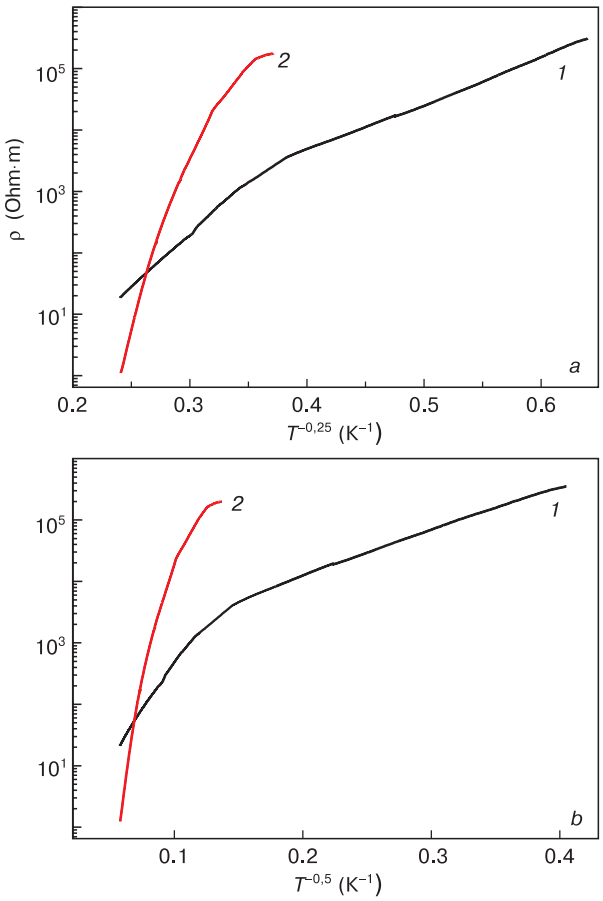

Figure 8. Temperature dependences of electrical resistivity for (*1*) undoped and (*2*) doped inhomogeneous ceramics in Mott's coordinates for (*a*) $\alpha = 0.25$ and (*b*) $\alpha = 0.5$ in Eq. (2).

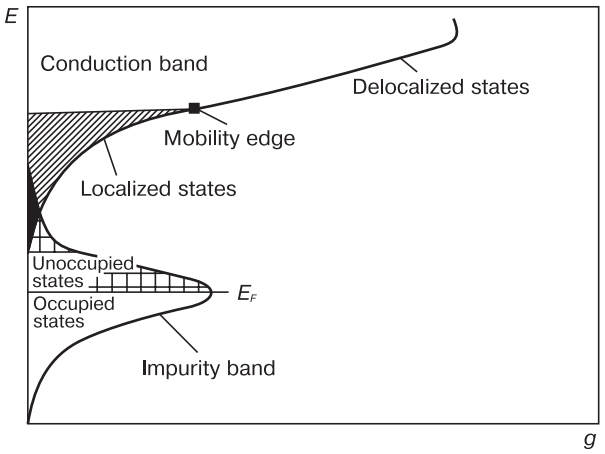

Figure 9. Diagram of the density of states for *n* conductivity doped ZnO as a function of electron energy for high intrinsic defect concentrations forming the impurity band and the tails of localized states near conduction band bottom.

development of large-scale potential profile. Therefore in accordance with earlier data [12, 41] the ρ(*T*) curves observed below 150 K in doped ZnO of n type of conductance can be described using the band energy diagram shown in Fig. 9. This diagram illustrates that the behavior of the ρ(*T*) curves for heating of an inhomogeneous specimen in the experimental temperature range can be interpreted as a sequential transition from Shklovskii-Efros' conductivity and then Mott's conductivity described by Eq. (2) which occur by hopping through localized "defect band" states to percolation conductivity described by Eq. (3) that is caused by the formation of large-scale potential roughness by intrinsic defects and impurities.

It should be noted that a combination of hopping conductivity attributed to Mott's law described by Eq. (2) at below 40 K with conventional band conductivity described by Eq. (1) at above 50 K was observed earlier in intrinsic ZnO single crystals [35] containing shallow intrinsic defects, e.g. interstitial zinc and/or oxygen vacancies which produce shallow donor levels with an ionization energy of about 0.05 eV.

4. Conclusion

The structure, type of doping Fe oxide and temperature were shown to affect the electrical properties of $(Fe_xO_y)_{10}(ZnO)_{90}$ ceramics ($0 \le x \le 3$; $1 \le y \le 4$) prepared using single- and two-stage synthesis methods in air. The doping agents were FeO, Fe_2O_3 and Fe_3O_4 iron oxides or (Fe_2O_3 + FeO) mixture. Carried out X-ray microfluorescent analysis, X-ray diffraction and Raman spectroscopy showed that at average iron concentrations of 1–3 at.% the ceramic specimens contain at least three phases: the $Zn_{1-\delta}Fe_\delta O$ solid solution with the iron content $\delta \le 0{,}81$ at.%, the $ZnFe_2O_4$ ferrite phase with a spinel structure and Fe_xO_y residual iron oxides. Scanning electron microscopy showed that the wurtzite phase grain size in the ceramic specimens decreases from several decades of microns for single-stage synthesis to submicron sizes for two-stage synthesis. Two-stage synthesis also improved the homogeneity of the grain size and composition distribution. Iron introduction in the ZnO crystal lattice produces deep donor centers with an activation energy of about 0.37 eV presumably due to the interaction of the iron ions with the intrinsic zinc oxide defects. The electrical resistivity *vs* temperature dependences ρ(*T*) for undoped zinc oxide in the 6–300 K range exhibit a variable activation energy indicating a heavily disordered structure and possible formation of large-scale potential relief. In the latter case an increase in the temperature of the ceramic specimens initiates a transition from Shklovskii-Efros' and Mott's hopping conductivity with a variable activation energy (6–30 K) to percolation conductivity (50–100 K) and band conductivity (above 200 K).

Acknowledgements

The Authors express their gratitude to the State Research Program "Physical Materials Science, New Materials and Technologies" (Belarus) for financial support.

References

1. Ivon A.I., Glot A.B., Lavrov R.I., Lu Z.-Ya. Grain resistivity in zinc oxide and tin dioxide varistor ceramics. *J. Alloys and Compounds*. 2014; 616: 372–377. https://doi.org/10.1016/j.jallcom.2014.07.178
2. Sawalha A., Abu-Abdeen M., Sedky A. Electrical conductivity study in pure and doped ZnO ceramic system. *Physica B*. 2009; 404: 1316–1320. https://doi.org/10.1016/j.physb.2008.12.017
3. Winarski D.J. Synthesis and characterization of transparent conductive zinc oxide thin films by sol-gel spin coating method: Thesis of Master of Science (Physics). Graduate College of Bowling Green, 2015, 87 p. http://rave.ohiolink.edu/etdc/view?acc_num=bgsu1434124579
4. Kopach V.R., Klepikova K.S., Klochko N.P., Khrypunov G.S., Korsun V.E., Lyubov V.M., Kirichenko M.V., Kopach A.V. Structure and properties of nanostructured ZnO arrays and ZnO/Ag nanocomposites fabricated by pulsed electrodeposition. *Semiconductors*. 2017; 51(3): 335–343. https://doi.org/10.1134/S1063782617030125
5. Zakhvalinskii V.S., Zakhvalinskaya M.N., Laiho R., Huhtinen H., Pilyuk E.A., Nekrasova Yu.S., Borisenko L.V. Preparation and magnetic properties of ZnO: Li, Fe. *Bulletin of Belgorod State University*. 2016; 6(42): 94–98. (In Russ.).
6. Jahafarova V.N., Orudzhev G.S., Guseinova S.S., Stempitskii V.R., Baranova M.S. Magnetic properties of vacancies and doped chromium in a ZnO crystal. *Semiconductors.* 2018; 52(8): 1047–1050. https://doi.org/10.1134/S1063782618080055
7. Gorokhova E.I., Rodnyi P.A., Chernenko K.A., Anan'eva G.V., Eron'ko S.B., Oreshchenko E.A., Khodyuk I.V., Lokshin E.P., Kunshina G.B., Gromov O.G., Lott K.P. Structural, optical, and scintillation characteristics of ZnO ceramics. *J. Opt. Technol.* 2011; 78(11): 753–760. https://doi.org/10.1364/JOT.78.000753
8. Kharchenko A.A., Bumai Yu.B., Gumarov A.I., Lukashevich M.G., Nuzhdin V.I., Khaibullin R.I., Odzhaev V.B. Electric and magnetic characteristics of Zink Oxide implanted with Co ions. *Bulletin of Belarusian State University: Ser. 1: Physics. Mathematics. Informatics*. 2014(1): 20–25. (In Russ.). http://elib.bsu.by/handle/123456789/113648
9. Parra-Palomino A., Singhal R., Perales Perez O., Dussan-Devia S., Tomar M.S. Low- Temperature Chemical Solution Synthesis and Characterization of Nanocrystalline Fe-doped ZnO. *NSTI-Nanotech*. 2007; 4: 297–300. https://briefs.techconnect.org/wp- content/volumes/Nanotech2007v4/pdf/1013.pdf
10. Kazeminezhad I., Saadatmand S., Yousefi R. Effect of transition metal elements on the structural and optical properties of ZnO nanoparticles. *Bull. Mater. Sci.*; 2016; 39(3): 719–724. https://doi.org/10.1007/s12034-016-1206-y
11. Jagannatha Reddy A., Kokila M.K., Nagabhushana H., Sharma S.C., Rao J.L., Shivakumara C., Nagabhushana B.M., Chakradhar R.P.S. Structural, EPR, photo and thermoluminescence properties of ZnO :

Fe nanoparticles. *Materials Chemistry and Physics*. 2012; 133(2–3): 876–883. https://doi.org/10.1016/j.matchemphys.2012.01.111

12. Silambarasan M., Saravanan S., Soga T. Raman and photoluminescence studies of Ag and Fe- doped ZnO. *Int. J. ChemTech Res.* 2015; 7(3): 1644–1650.
13. Makino T., Segawa Y., Tsukazaki A., Saito H., Takeyama S., Akasaka S., Nakahara K., Kawasaki M. Magneto-photoluminescence of charged excitons from MgxZn1-xO/ZnO heterojunctions. *Phys. Rev. B*. 2013; 87(8): 085312-1-7. https://doi.org/10.1103/PhysRevB.87.085312
14. Shao Q., Liao F., Ruotolo A. Magnetic-polaron-induced enhancement of surface Raman scattering. *Scientific Reports*, 2016; 6: 19025. https://doi.org/10.1038/srep19025
15. Goldsmith H.J. Introduction to the Thermoelectricity. Berlin: Springer Berlin Heidelberg, 2016, 233 p. https://doi.org/10.1007/978-3-642-00716-3
16. Roychowdhury A., Mishra A.K., Pati S.P., Das D. Synthesis and characterization of multifunctional Fe3O4–ZnO nanocomposites. *AIP Conf. Proc.* 2012; 1447(1): 283–284. https://doi.org/10.1063/1.4709990
17. Zou P., Hong X., Chu X., Li Y., Liu Y. Multifunctional Fe3O4/ZnO nanocomposites with magnetic and optical properties. *J. Nanosci. Nanotechnol.* 2010; 10(3): 1992–1997. https://doi.org/10.1166/jnn.2010.2098
18. Hasanpour A., Niyaifar M., Asan M., Amighian J. Synthesis and characterization of Fe3O4 and ZnO nanocomposites by the sol-gel method. *J. Magn. Magn. Mater.* 2013; 334: 41–44. https://doi.org/10.1016/j.jmmm.2013.01.016
19. Roychowdhurya A., Pati S.P., Mishra A.K., Kumar S., Das D. Magnetically addressable fluorescent Fe3O4/ZnO nanocomposites: structural, optical and magnetization studies. *J. Phys. Chem. Solids*. 2013; 74(6): 811–818. https://doi.org/10.1016/j.jpcs.2013.01.012
20. Karpova S.S., Moshnikov V.A., Myakin S.V., Kolovangina E.S. Surface functional composition and sensor properties of ZnO, Fe2O3 and ZnFe2O4. *Semiconductors*. 2013; 47(3): 392–395. https://doi.org/10.1134/S1063782613030123
21. Janotti A., Van de Walle C.G. Fundamentals of zinc oxide as a semiconductor. *Rep. Prog. Phys.* 2009; 72(12): 1–29. https://doi.org/10.1088/0034-4885/72/12/126501
22. Janotti A., Van de Walle C.G. Native point defects in ZnO. Phys. Rev. B, 2007; 76(16): 1–22. https://doi.org/10.1103/PhysRevB.76.165202
23. Wu X.L., Siu G.G., Fu C.L., Ong H.C. Photoluminescence and cathodoluminescence studies of stoichiometric and oxygen-deficient ZnO films. *Appl. Phys. Lett.,* 2001; 78(16): 2285–2287. https://doi.org/10.1063/1.1361288
24. Hausmann A. The cubic field parameter of 6S5/2 ions in zinc oxide crystals. *Solid State Commun.* 1968; 6(7): 457–459. https://doi.org/10.1016/0038-1098(68)90054-9
25. Walsh W.M., Rupp L.W. Paramagnetic resonance of trivalent Fe57 in zinc oxide. *Phys. Rev.*, 1962; 126(3): 952–955. https://doi.org/10.1103/PhysRev.126.952
26. Jiang Y., Giles N.C., Halliburton L.E. Persistent photoinduced changes in charge states of transition-metal donors in hydrothermally grown ZnO crystals. *J. Appl. Phys.*, 2007; 101(9): 093706-1-8. https://doi.org/10.1063/1.2723872
27. Schmidt-Mende L., MacManus-Driscoll J.L. ZnO – nanostructures, defects, and devices *Materials Today*, 2007; 10(5): 40–48. https://doi.org/10.1016/S1369-7021(07)70078-0
28. Rodríguez-Carvajal J. Recent advances in magnetic structure determination by neutron powder diffraction. *Physica B: Condensed Matter*, 1993; 192(1–2): 55–69. https://doi.org/10.1016/0921-4526(93)90108-I
29. Rancourt D.G. Accurate site population form Mössbauer spectroscopy. *Nucl. Instr. Meth. B*, 1989; 44(2): 199–210. https://doi.org/10.1016/0168-583X(89)90428-X
30. Stewart S.J., Figueroa S.J.A., Sturla M.B., Scorzelli R.B., García F., Requejo F.G. Magnetic ZnFe2O4 nanoferrites studied by X-ray magnetic circular dichroism and Mössbauer spectroscopy. *Physica B*: *Condensed Matter*, 2007; 389(1): 155–158. https://doi.org/10.1016/j.physb.2006.07.045
31. Bødker F., Mørup S. Size dependence of the properties of hematite nanoparticles. *Europhys. Lett.*, 2000; 52(2): 217–223. https://doi.org/10.1209/epl/i2000-00426-2
32. Shklovskii B.I., Efros A.L. *Electronic properties of doped semiconductors*. Berlin; Heidelberg: Springer-Verlag, 1984, 388 p. https://doi.org/10.1007/978-3-662-02403-4
33. Kohan A.F., Ceder G., Morgan D., Van de Walle C.G. First-principles study of native point defects in ZnO. *Phys. Rev. B*, 2000; 61(22): 15019–15027. https://doi.org/10.1103/PhysRevB.61.15019
34. Chiu S.P., Lin Y.H., Lin J.J. Electrical conduction mechanisms in natively doped ZnO nanowires. Nanotechnology, 2009; 20(1): 015203-1–8. https://doi.org/10.1088/0957-4484/20/1/015203
35. Lien C.C., Wu C.Y., Li Z.Q., Lin J.J. Electrical conduction processes in ZnO in a wide temperature range 20–500 K. *J. Appl. Phys.*, 2011; 110(6: 063706-1-7. https://doi.org/10.1063/1.3638120
36. Quemener V., Vines L., Monakhov E.V., Svensson B.G. Iron related donor-like defect in zinc oxide. *Appl. Phys. Lett.*, 2013; 102(23): 232102-1-3. https://doi.org/10.1063/1.4809941
37. Mott N.F., Davis E.A. Electronic processes in non-crystalline materials. Oxford: Clarendon Press; New York: Oxford University Press, 1979, 590 p.
38. Von Wenckstern H., Schmidt H., Grundmann M., Allen M.W., Miller P., Reeves R.J., Durbin S.M. Defects in hydrothermally grown bulk ZnO. *Appl. Phys. Lett*., 2007; 91(2): 022913-1-3. https://doi.org/10.1063/1.2757097
39. Shik A.Ya. Hall effect and electron mobility in inhomogeneous semiconductors. *JETP Lett.*, 1974; 20(1): 5–7. http://www.jetpletters.ac.ru/ps/1783/index.shtml
40. Kasiyan V.A., Nedeoglo D.D., Simashkevich A.V., Timchenko I.N. Electron mobility in heavily doped strongly compensated ZnSe crystals. *Phys. Status Solidi B*, 1986; 136(1): 341–347. https://doi.org/10.1002/pssb.2221360138
41. Kagan V.D. Electron capture by charged impurities in semiconductors under conditions of spatial diffusion. *Phys. Solid State*, 2005; 47(3): 446–450. https://doi.org/10.1134/1.1884703